A Nd@C_{82}–polymer interface for efficient and stable perovskite solar cells

https://doi.org/10.1038/s41586-025-08961-9

Received: 27 July 2024

Accepted: 1 April 2025

Yuexin Lin[1,15], Zhichao Lin[2,15], Shili Lv[3,15], Yuan Shui[1,15], Wenjing Zhu[1,15], Zuhong Zhang[4], Wenhan Yang[1], Jinbo Zhao[4], Hao Gu[5], Junmin Xia[6], Danning Wang[3], Fenqi Du[1], Annan Zhu[5], Jin Liu[1], Hairui Cai[1], Bin Wang[1], Nan Zhang[1], Haibin Wang[7], Xiaolong Liu[8], Tao Liu[9], Chuncai Kong[1], Di Zhou[9], Shi Chen[5], Zhimao Yang[1], Tao Li[10], Wei Ma[10], Guojia Fang[11], Luis Echegoyen[12,13], Guichuan Xing[5]✉, Shengchun Yang[1,10]✉, Tao Yang[1]✉, Wenting Cai[3]✉, Meng Li[4]✉, Wei Huang[14] & Chao Liang[1]✉

An important challenge in the commercialization of perovskite solar cells (PSCs) is the simultaneous attainment of high power conversion efficiency (PCE) and high stability. Using polymer interfaces in PSCs can enhance durability by blocking water and oxygen and by suppressing ion interdiffusion, but their electronic shielding poses a challenge for efficient and stable PSCs[1–3]. Here we report a magnetic endohedral metallofullerene Nd@C_{82}–polymer coupling layer, which features ultrafast electron extraction and in situ encapsulation, thereby promoting homogeneous electron extraction and suppressing ion interdiffusion. The Nd@C_{82}–polymer coupling layer in PSCs exhibited a PCE of 26.78% (certified 26.29%) and 23.08% with an aperture area of 0.08 cm^2 and 16 cm^2 (modules), respectively. The unencapsulated devices retained about 82% of the initial PCE after 2,500 h of continuous 1-sun maximum power point operation at 65 °C.

Metal halide perovskite solar cells (PSCs) with inverted (p-i-n) structures have achieved certified power conversion efficiencies (PCEs) of up to 26.7%, and they possess superior long-term operational stability under harsh stresses compared with the n-i-p counterparts[4–7]. Further improvements in the performance and stability of inverted PSCs require the rational management of carrier extraction processes and internal encapsulation between charge transport layers and the perovskite absorber[8–11].

Recently, self-assembled monolayers (SAMs), such as the (2-(4-(bis(4-methoxyphenyl)amino)phenyl)-1-cyanovinyl)phosphonic acid series, have been widely used in inverted PSCs[8]. In these studies, the SAMs serve as the hole transporting layer (HTL), which facilitates the subsequent growth of high-quality perovskite films while suppressing interfacial non-radiative recombination, thus enabling efficient hole extraction[9,12,13].

Substantial efforts have been made to optimize the interface between the electron transporting layer (ETL) and the perovskite layer. Among them, polymer-based materials have demonstrated exceptional internal encapsulation features, providing excellent self-healing properties and improved stability against moisture, light and heat, which have not been attainable with small molecular defect passivating agents[3,14–16]. However, when the polymer layer is sufficiently thick, its pronounced electronic shielding effect greatly suppresses charge extraction, thus limiting the performance of inverted PSCs. Consequently, conventional ETLs, such as [6,6]-phenyl-C_{61}-butyric acid methyl ester (PCBM) or C_{60}, are not compatible with balanced electron extraction because SAMs with a conjugated structure show faster hole extraction rates than the electron extraction rate of PCBM or C_{60} in the polymer internal encapsulation-based inverted PSCs[17–21]. Therefore, it is crucial to develop strategies that can enhance electron extraction abilities while maintaining the excellent in-situ encapsulation and self-healing properties of polymer-based agents in inverted PSCs.

Here we propose that the aforementioned challenges can be addressed by incorporating an ultrafast electron-selective layer (ESL), which matches the kinetics of the HTL and thereby enables an efficient and balanced extraction of charge carriers. To fulfil the requirement of ultrafast ESL, we demonstrated the efficacy of an endohedral metallofullerene–polymer coupling ESL, Nd@C_{82}, with both intramolecular short transfer channels and electromagnetic-coupled transmitter for enhanced electron extraction ability and efficiency through

---

[1] MOE Key Laboratory for Nonequilibrium Synthesis and Modulation of Condensed Matter, School of Physics, National Innovation Platform (Center) for Industry-Education Integration of Energy Storage Technology, Xi'an Jiaotong University, Xi'an, People's Republic of China. [2] College of Material Engineering, Fujian Agriculture and Forestry University, Fuzhou, People's Republic of China. [3] School of Chemistry, Xi'an Jiaotong University, Xi'an, People's Republic of China. [4] Key Lab for Special Functional Materials of Ministry of Education, School of Nanoscience and Materials Engineering, Henan University, Kaifeng, People's Republic of China. [5] Joint Key Laboratory of the Ministry of Education, Institute of Applied Physics and Materials Engineering, University of Macau, Avenida da Universidade, Macau, People's Republic of China. [6] State Key Laboratory of Organic Electronics and Information Displays, Nanjing University of Posts and Telecommunications, Nanjing, People's Republic of China. [7] Institute of Advanced Ceramics, Henan Academy of Sciences, Zhengzhou, People's Republic of China. [8] State Key Laboratory of Crystal Materials & Institute of Crystal Materials, Shandong University, Jinan, People's Republic of China. [9] Key Laboratory of Multifunctional Materials and Structures, Ministry of Education, School of Electronic Science and Engineering, Xi'an Jiaotong University, Xi'an, People's Republic of China. [10] State Key Laboratory for Mechanical Behavior of Materials, School of Materials Science and Engineering, Xi'an Jiaotong University, Xi'an, People's Republic of China. [11] Key Laboratory of Artificial Micro/Nano Structures of Ministry of Education, School of Physics and Technology, Wuhan University, Wuhan, People's Republic of China. [12] Department of Chemistry, The University of Texas at El Paso, El Paso, TX, USA. [13] Institute of Chemical Research of Catalonia (ICIQ), The Barcelona Institute of Science and Technology, Tarragona, Spain. [14] Institute of Flexible Electronics (IFE), Northwestern Polytechnical University (NPU), Xi'an, People's Republic of China. [15] These authors contributed equally: Yuexin Lin, Zhichao Lin, Shili Lv, Yuan Shui, Wenjing Zhu. ✉e-mail: gcxing@um.edu.mo; ysch1209@mail.xjtu.edu.cn; taoyang1@xjtu.edu.cn; caiwt88@xjtu.edu.cn; mengli@henu.edu.cn; chaoliang@xjtu.edu.cn

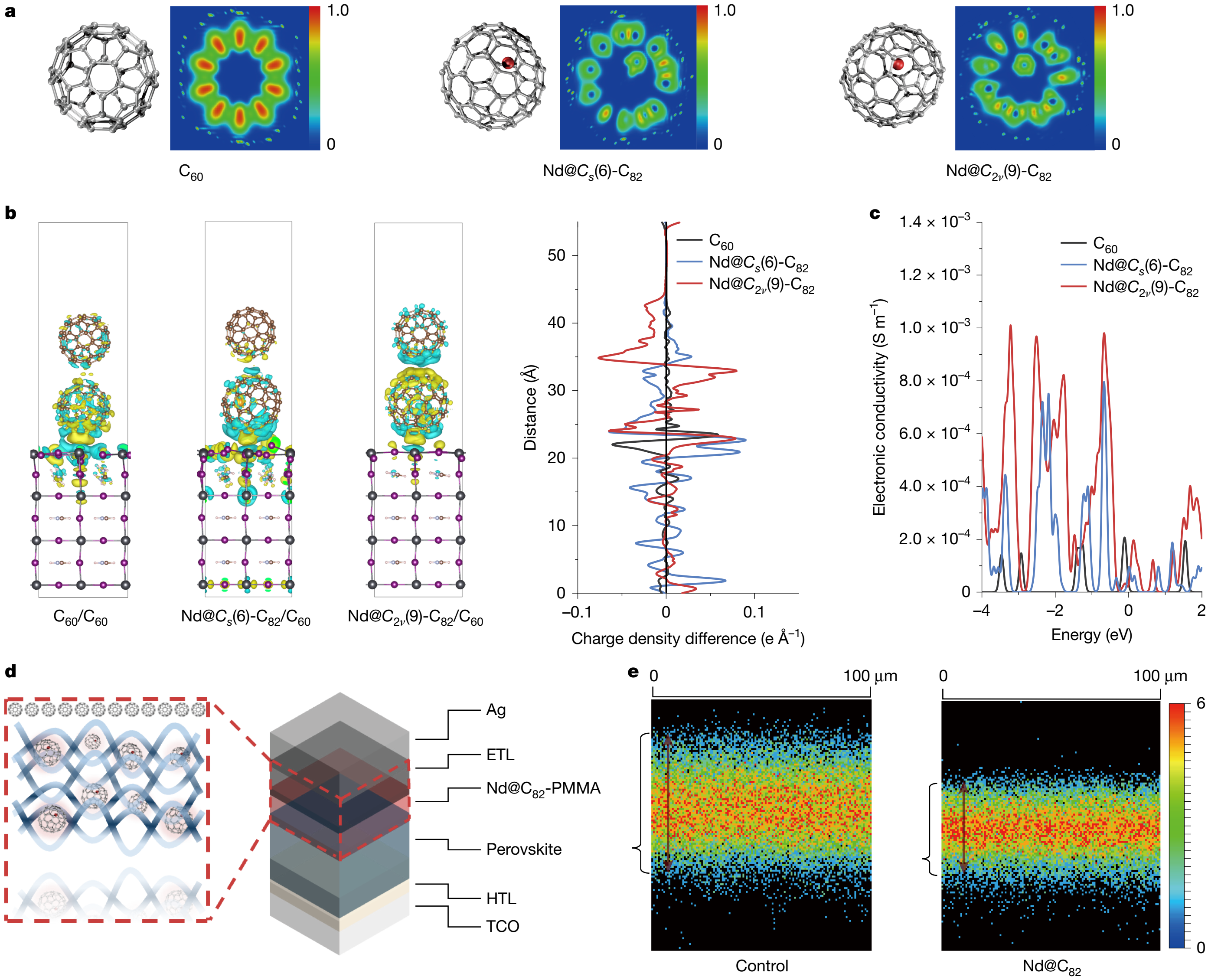

Fig. 1 | Endohedral magnetic metallofullerene $Nd@C_{82}$–PMMA coupling layer facilitates ultrafast electron extraction and lead immobility. **a**, Molecular structure of C_{60}, $Nd@C_s(6)\text{-}C_{82}$ and $Nd@C_{2v}(9)\text{-}C_{82}$ and their respective ELFs. **b**, Charge density difference distributions of perovskite (with PbI_2-terminated $FAPbI_3$ surface)/fullerene slabs. **c**, The calculated electronic conductivity of $Nd@C_{82}$. **d**, Schematic of the device configuration of a typical inverted perovskite solar cell (PSC) with $Nd@C_{82}$–PMMA coupling layer. TCO, transparent conducting oxide; HTL, hole transport layer; PMMA, polymethyl methacrylate; ETL, electron transport layer. **e**, Cross-sectional TOF-SIMS mapping of control and $Nd@C_{82}$-based device (PbI^+) after 1,008 h of ageing at 85 °C in a nitrogen atmosphere, respectively. The span of sputtering time in these images is from 0 s to 900 s.

interfacial polarization. The $Nd@C_{82}$–PMMA (polymethyl methacrylate) coupling layer ensured homogeneous ultrafast electron extraction and also excellent band alignment with the perovskite layer. As a result, the inverted PSCs had aperture areas of 0.08 cm^2 and 16.0 cm^2 (modules) with PCEs of 26.78% (certified 26.29%) and 23.08%, respectively. The stability results showed that the unencapsulated target PSCs retained 95% of their initial PCE after 1,750 h (85 °C, ISOS-D-2I, where ISOS is International Summit on Organic Photovoltaic Stability[22]) and retained 82% of the initial PCE after operating in maximum power point tracking (MPPT) at 65 °C (ISOS-L-3) for 2,500 h under 1-sun illumination. Furthermore, the encapsulated $Nd@C_{82}$-based devices show almost no efficiency reduction under the damp heat test conditions (ISOS-D-3) over 1,000 h.

Ultrafast electron extraction design

The detailed synthesis, isolation and characterization of two monometallofullerenes $Nd@C_{82}$ (I, II) isomers are shown in Supplementary Note 1. The crystallographic study unambiguously identified $Nd@C_{82}$ (I) as $Nd@C_{2v}(9)\text{-}C_{82}$ and $Nd@C_{82}$ (II) as $Nd@C_s(6)\text{-}C_{82}$, respectively. The molecular structures of two $Nd@C_{82}$ isomers with C_{2v} and C_s symmetries are shown in Fig. 1a. In $Nd@C_{82}$, a single metal ion Nd(III) is located inside a C_{82} fullerene cage. The dipole moments of C_{60}, $Nd@C_s(6)\text{-}C_{82}$ and $Nd@C_{2v}(9)\text{-}C_{82}$ are calculated to be approximately 0 D, 3.2 D and 3.3 D, respectively, which align well with the experimentally measured results by relative dielectric constant (Supplementary Note 2 and Supplementary Fig. 10). Unlike non-polar C_{60} molecules with weak dispersion forces, polar $Nd@C_{82}$ molecules generate strong attractive dipole forces through the orientation of opposite poles, thereby building a permanent strong electric field mediated by the $Nd@C_{82}$ interface[23–25] (Supplementary Note 2). According to the electron localization function (ELF) of $Nd@C_{82}$, the fullerene cage exhibits higher electron localization (negative charge) compared with the metal Nd(III), suggesting an intramolecular electron transfer (ET) from the fullerene cage to the internal Nd(III) and subsequently to the

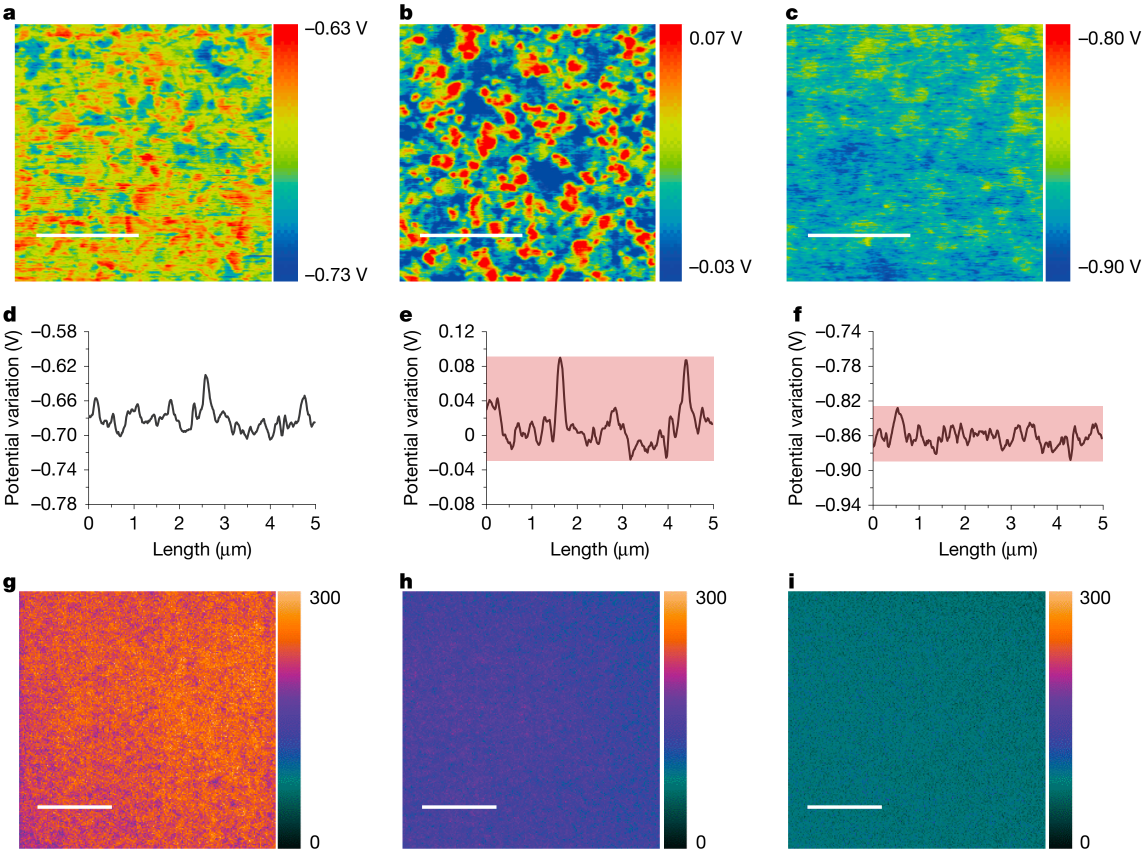

Fig. 2 | Electronic and optical properties of perovskite films with Nd@C_{82}–PMMA coupling layer incorporation. **a**–**c**, KPFM surface potential images for the neat perovskite film (**a**), perovskite/C_{60} film (**b**) and perovskite/Nd@C_{82}/C_{60} film (**c**). **d**–**f**, Surface potential variation of the neat perovskite film (**d**), perovskite/C_{60} film (**e**) and perovskite/Nd@C_{82}/C_{60} film (**f**). **g**–**i**, PL mapping images for the neat perovskite film (**g**), perovskite/C_{60} film (**h**) and perovskite/Nd@C_{82}/C_{60} film (**i**). Scale bars, 2 μm (**a**–**c**); 10 μm (**g**–**i**).

fullerene cage[26]. To further verify the Nd-induced intramolecular ET, electron paramagnetic resonance (EPR) spectra were used to detect paramagnetic signals. The peak ($g = 1.92$) observed for Nd@C_{82} (Supplementary Fig. 5) indicated that Nd-induced ultrafast intramolecular ET could be achieved by the coupling between endohedral metals and the fullerene cages, resulting in intramolecular shortened transfer channels[27]. More importantly, the endohedral metal Nd inside the C_{82} cages can spontaneously move from below to above in the cage in the built-in electric field, which ensures a strong permanent charge extraction ability (Supplementary Note 3).

To explain the effect of Nd@C_{82}–PMMA on the perovskite surface chemistry and electronic band structure, X-ray photoemission spectroscopy (XPS) measurements were conducted on control and Nd@C_{82}-deposited perovskite films. The spectrum of Nd@C_{82}-deposited perovskite films exhibited an Nd 3*d* peak located at 1,003.9 eV, whereas the control film without Nd@C_{82} deposition showed no Nd $3d_{3/2}$ characteristic peaks[28]. These results showed that the successful incorporation of Nd@C_{82} (with about 10 nm thickness; Supplementary Note 4 and Supplementary Figs. 12 and 13) into the device does not markedly change the perovskite films (Supplementary Figs. 14–17). After Nd@C_{82}–PMMA coupling ultrafast ESL incorporation between the perovskite layer and ETL, a dense bilayer (Nd@C_{82}–PMMA/C_{60}) stack would be formed (Supplementary Figs. 18 and 19). Figure 1b presents the perovskite/Nd@C_s(6)-C_{82}/C_{60} and perovskite/Nd@C_{2v}(9)-C_{82}/C_{60} models. The obvious electron delocalization over Nd@C_{82} indicates an effective vertical ET from the perovskite layer (with both with PbI_2-terminated and FAI-terminated $FAPbI_3$ surface) to the ETL through the Nd@C_{82} layer (Supplementary Fig. 20). More importantly, the delocalized electrons are located at the perovskite/ETL interface, which results in an enhanced local built-in electric field by strong dipole interface[10,29] (Supplementary Fig. 21). We also quantified the electronic conductivity of Nd@C_{82} and C_{60}, respectively, through the Boltzmann transport equation[30], as shown in Fig. 1c. Nd@C_{82} exhibits a maximum varying axis average electronic conductivity (1.0×10^{-3} S m^{-1}) approximately five times higher than that of C_{60} (2.1×10^{-4} S m^{-1}) (ref. 31), with slight differences in different directions (Supplementary Figs. 22 and 23). Those static calculation results suggest that the electrons could transfer more quickly through Nd@C_{82} than through C_{60}, because of Nd-induced ultrafast ET by intramolecular transfer channels.

Notably, Nd@C_{2v}(9)-C_{82} exhibits stronger electron delocalization and higher electronic conductivity with respect to Nd@C_s(6)-C_{82} because of its higher cage symmetry and the different motional behaviour of the Nd ion inside the fullerene cages (Supplementary Note 5). Therefore, unless otherwise stated, Nd@C_{2v}(9)-C_{82} was used to fabricate all Nd@C_{82}-based devices and samples discussed in the present work. Defining this inserted layer as Nd@C_{82}–PMMA in Fig. 1d, we emphasize the presence of thick PMMA that confers the positive properties to the suppression of ion diffusion without chemical interactions (Supplementary Note 6). Moreover, the contact angle to water is enhanced after introducing Nd@C_{82}–PMMA because of the moisture resistance of the polymer[1,2,32–34] (Supplementary Fig. 26). For simplicity, Nd@C_{82}–PMMA used in this study is abbreviated as Nd@C_{82}.

The diffusion of lead ions from the perovskite layer to the ETL heterointerface was characterized by time-of-flight secondary ion mass spectrometry (TOF-SIMS), and the results indicated that there was almost no interdiffusion between lead ions and electrodes of the

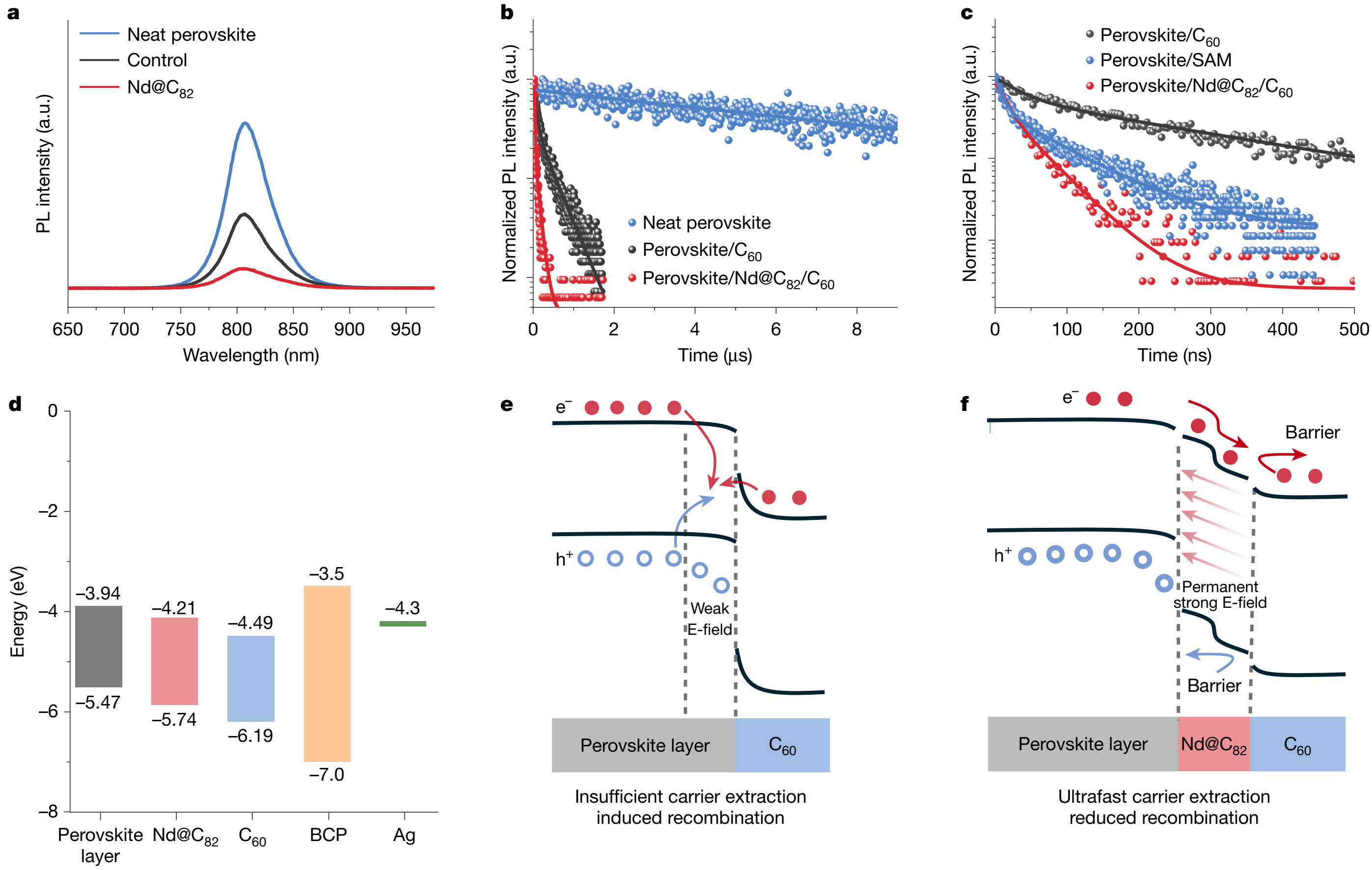

Fig. 3 | Nd@C_{82}–PMMA coupling layer for balanced charge carrier transport. **a**, Steady-state PL spectra of neat perovskite, control (perovskite/C_{60}) and Nd@C_{82} (perovskite/Nd@C_{82}/C_{60}) film (excitation from the front side). **b**, TRPL spectra of neat perovskite, control (perovskite/C_{60}) and Nd@C_{82} (perovskite/Nd@C_{82}/C_{60}) film (excitation from the front side). **c**, TRPL spectra of perovskite/C_{60}, perovskite/SAM and perovskite/Nd@C_{82}/C_{60} film (excitation from the front side). **d**, Band alignment between perovskite and ETL. **e**,**f**, Energy diagram for control (**e**) and Nd@C_{82}-based PSCs (**f**) (the structure is shown at the bottom). a.u., arbitrary units.

Nd@C_{82}-based device after 1,008 h of ageing at 85 °C in a nitrogen atmosphere. By contrast, the interdiffusion between lead ions and electrodes was detected for the control devices, which is detrimental to the long-term operation stability of the devices (Fig. 1e). It is important to emphasize that the suppression of ion diffusion is not specific to lead ions. Similar suppression was observed for the diffusion of carbon, iodine and silver ions. This result indicates that the enhanced thermal stability of the Nd@C_{82}-based device can be attributed to the protective role of the interpenetrating network structure formed by polymer (PMMA). This network effectively impedes ion diffusion under ageing conditions, thereby contributing to the overall stability of the devices (Supplementary Figs. 27 and 28).

Properties of Nd@C_{82}-incorporated films

We assessed the homogeneity of the films by Kelvin probe force microscopy (KPFM) mapping, and the surface potential variation was comparable to that of previously reported conventional perovskite films[35,36]. After incorporation of the Nd@C_{82} ESL between the perovskite film and the ETL (C_{60}), the strong dipole force induced ultrafast intramolecular ET. Furthermore, Nd@C_{82}–PMMA, with a relatively high electroconductivity and smoothing effect that helps to disperse the electric field, thereby preventing the concentration of electric charges at localized points and thus reduce the surface potential, would allow the contact potential variation (CPV) to be more homogeneous[37,38] (Fig. 2a–c and Supplementary Note 7). The CPV of C_{60} and Nd@$_{82}$/C_{60}, measured by KPFM, was reduced from 118 mV to 64 mV (Fig. 2d–f). Photoluminescence (PL) mapping of perovskite films was performed, which shows that the Nd@C_{82}/C_{60} film was more uniform and showed reduced intensity, compared with that of a C_{60} film (Fig. 2g–i and Supplementary Fig. 30), which might be beneficial to homogeneous ultrafast charge carrier extraction in the resulting films[39].

To study the underlying mechanism of improved electron extraction resulting from Nd@C_{82}, we evaluated the electrical conductance (G) by measuring the current–voltage (I–V) curves of glass/ITO/without or with Nd@C_{82} (0.5-2.0 mg ml^{-1})/C_{60}/Ag structure. Nd@C_{82}–1.0 mg ml^{-1}/C_{60} shows the highest electrical conductance (0.41 Ω^{-1}), which can be attributed to the strong electron-withdrawing properties of the endohedral metals Nd(III), but further improvement of the Nd@C_{82} concentration leads to aggregation, causing a slight decrease in conductance (Supplementary Fig. 31 and Supplementary Table 2). Considering the benefits of the instantaneous dipole moments of C_{82} cage and electronic properties of Nd(III), we speculate that intramolecular ET occurs from the fullerene cage to the internal Nd(III) and subsequently to the fullerene cage, which is consistent with the above ELF calculations and EPR spectra. We then calculated the electron mobility (μ_e) of C_{60} and Nd@C_{82} (0.5–2.0 mg ml^{-1})/C_{60} by the space-charge-limited current (SCLC) model of ITO/without or with Nd@C_{82} (0.5–2.0 mg ml^{-1})/C_{60}/Ag structure. The μ_e of Nd@C_{82} (1.0 mg ml^{-1})/C_{60} is 9.09 × 10^{-4} cm^2 V^{-1} s^{-1}, significantly larger than that for C_{60} (4.10 × 10^{-4} cm^2 V^{-1} s^{-1}). Thus, these results indicate that Nd@C_{82} at 1.0 mg ml^{-1} helps to retain the electron extraction when incorporated into the perovskite/ETL, as shown by

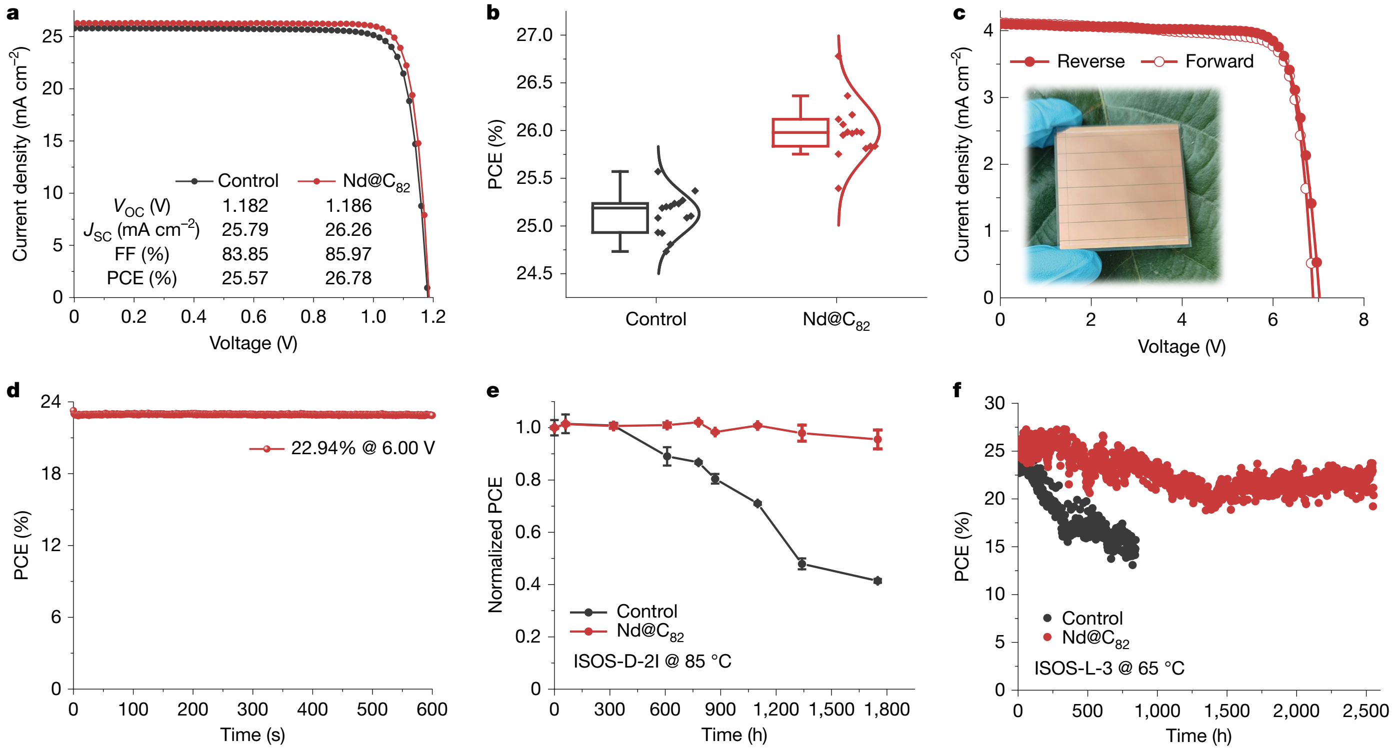

Fig. 4 | Photovoltaics and stability of Nd@C$_{82}$-based PSCs and modules. **a**, *J*–*V* curves of the champion control and Nd@C$_{82}$-based PSCs under 1-sun (100 mW cm^{-2}) illumination. **b**, The statistics of PCE values obtained from *J*–*V* characteristic for the control and Nd@C$_{82}$-based devices (15 devices for each type; the box outline represents the standard deviation of the data). **c**, *J*–*V* curves of champion modules (25 cm^2) based on Nd@C$_{82}$. **d**, The stabilized PCE of champion modules based on Nd@C$_{82}$. **e**, ISOS-D-2I device stability during storage at 85 °C for 1,750 h (where ISOS is International Summit on Organic Photovoltaic Stability, five devices for each type). The error bars denote standard deviation. In cases where error bars are not visible, they are smaller than the symbol size. **f**, MPPT stability of control and Nd@C$_{82}$-based PSCs under simulated 1-sun illumination at 50% relative humidity and temperature of 65 °C (ISOS-L-3).

enhanced μ_e (Supplementary Fig. 32, Supplementary Table 3 and Supplementary Note 8).

Electron extraction properties

The electron extraction properties of Nd@C$_{82}$/C$_{60}$ were studied by observing the PL quenching of the perovskite film with C$_{60}$ or Nd@C$_{82}$/C$_{60}$ (Fig. 3a and Supplementary Note 9). We noticed that the PL intensity of perovskite/Nd@C$_{82}$/C$_{60}$ is weaker than that of perovskite/C$_{60}$, indicating that Nd@C$_{82}$/C$_{60}$ is a more effective electron extractor than that of C$_{60}$ (ref. 18). Time-resolved PL (TRPL) spectra were also conducted to show the influence of Nd@C$_{82}$ on ultrafast photogenerated carrier extraction at the interface between perovskite and ETL. After the exponential fitting, we calculated the effective PL lifetimes as 7.78 µs, 127.57 ns and 26.28 ns for the neat perovskite film, perovskite/C$_{60}$ and perovskite/Nd@C$_{82}$/C$_{60}$, respectively (Fig. 3b and Supplementary Note 10). The reduced lifetime indicates that the presence of Nd@C$_{82}$ promotes the electron-selective extraction through internal Nd(III)-induced shortened transfer channels[27]. We then estimated the extraction ability of C$_{60}$ and Nd@C$_{82}$/C$_{60}$ according to the time to the flat region calculated from the differential lifetime of exponential fitting curves[40], in which the shift of the differential lifetime to the plateau represents the end of charge carrier transformation (Supplementary Fig. 34 and Supplementary Note 11). The Nd@C$_{82}$/C$_{60}$ shows a better electron extraction ability than C$_{60}$, which can be mainly attributed to the Nd(III)-induced improved intramolecular ET. More importantly, because of electron–hole balanced extraction with either ETL or HTL, equal extraction efficiencies ($\eta_{\text{extraction}}$) for ETL and HTL would suppress carrier recombination at the perovskite/ETL interface (Supplementary Figs. 35–38). Based on these results, the calculated $\eta_{\text{extraction}}$ for SAM and Nd@C$_{82}$/C$_{60}$ are fairly consistent, demonstrating the accomplishment of electron–hole balanced extraction kinetics (Fig. 3c, Supplementary Tables 4 and 5 and Supplementary Note 12).

Subsequently, we performed depth profiles ultraviolet photoelectron spectroscopy (UPS) combining the corresponding optical bandgap to investigate the band alignment between perovskite and ETL to explain the electronic structure of the Nd@C$_{82}$ interface layer. Figure 3d shows the energy diagrams of PSCs with Nd@C$_{82}$. We identified a type II band alignment with minimal energy level mismatch between the perovskite and ETL, which could substantially reduce the insufficient carrier extraction-induced recombination at the heterointerface. This reduction is because of the permanent strong electric field mediated by the Nd@C$_{82}$ polarized interface, facilitating more efficient carrier separation and extraction (Fig. 3e,f, Supplementary Figs. 39–41 and Supplementary Table 5).

Performance of PSCs and modules

To study the photovoltaic performance of Nd@C$_{82}$-based devices, we first fabricated small-area inverted PSCs (0.08 cm^2) with a configuration of ITO/HTL/perovskite/with or without Nd@C$_{82}$/C$_{60}$/BCP/Ag. The concentration of Nd@C$_{82}$ was optimized to be 1 mg ml^{-1} (in 1 mg ml^{-1} PMMA chlorobenzene solution) to achieve the best performance (Supplementary Figs. 42–46 and Supplementary Tables 6–8). Detailed fabrication procedures can be found in the Supplementary Information. The current density–voltage (*J*–*V*) curves of champion devices based on Nd@C$_{82}$-based are shown in Fig. 4a, in which the Nd@C$_{82}$-based devices exhibited an increased PCE from 25.57% to 26.78%, with an open-circuit voltage (V_{OC}) of 1.186 V, fill factor (FF) of 85.97% and a short-circuit current density (J_{SC}) of 26.26 mA cm^{-2}. A well-matched current response is observed in the external quantum efficiency (EQE) spectra (Supplementary Fig. 47). Analysis of device statistics for both control and Nd@C$_{82}$-based PSCs showed a substantial enhancement in PCE, primarily because of increased J_{SC} and FF (Fig. 4b and Supplementary Fig. 43). We attribute this improvement to the enhanced electron extraction induced by Nd@C$_{82}$ in the resulting PSCs, rather than defect passivation (Supplementary Note 13). We sent one of the unencapsulated Nd@C$_{82}$-based devices to an accredited independent photovoltaic test laboratory (National PV Industry Measurement and Testing Center) for certification, and the device delivered a certified PCE of 26.29%, with V_{OC} of 1.185 V, FF of 83.70% and J_{SC} of 26.51 mA cm^{-2}. As our devices are not externally encapsulated, we attribute this slight drop to mechanical damage during transportation. This performance is one of the highest values reported to date for PSCs with inverted structure (Supplementary Table 9). The stabilized PCE was 26.15% after MPPT for 300 s (certified) (Supplementary Fig. 49). To further validate the feasible application of the Nd@C$_{82}$–PMMA coupling layer in scalable PSCs, we fabricated a PSC module with an active area of around 16.0 cm^2 and tested its J–V characteristics (Fig. 4c). The PCE of the module with six subcells reached 23.08%, with a J_{SC} of 4.10 mA cm^{-2}, a V_{OC} of 7.02 V and an FF of 80.18%. The stabilized PCE of the module was 22.94% after MPPT for 600 s (Fig. 4d). We sent one of the modules to an independent laboratory (Shanghai Institute of Microsystem and Information Technology) for certification, and a PCE of 22.03% was obtained from the reverse J–V scan (Supplementary Fig. 50), demonstrating excellent reproducibility (Supplementary Fig. 51).

The thermal stability of both control and Nd@C$_{82}$-based devices was evaluated following ISOS-D-2I protocols, in which the devices were subjected to dark storage at 85 °C and periodically tested. The unencapsulated Nd@C$_{82}$-based devices retained 95% of their initial PCE after 1,750 h (Fig. 4e and Supplementary Fig. 52). To further evaluate operating stability, we performed ISOS-L-3 testing under MPPT under 1 sun for a device operating in ambient air. After more than 2,500 h of continuous operation under 1-sun illumination at 65 °C, the unencapsulated Nd@C$_{82}$-based device retained 82% of its initial PCE (Fig. 4f and Supplementary Fig. 52). A comparison with other PSCs tested following the ISOS-L-3 protocol is presented in Supplementary Table 10. Moreover, we placed encapsulated devices in a chamber to conduct the damp heat test (85 °C and 85% relative humidity) following the ISOS-D-3. The Nd@C$_{82}$-based devices display almost no efficiency reduction under the damp heat test conditions (ISOS-D-3) over 1,000 h under damp heat ageing, whereas the control devices retained only 60.6% of their initial PCEs within the same ageing time (Supplementary Figs. 52 and 53). These stability improvements are attributed to the suppression interdiffusion effects by the interpenetrating network of polymer and insulating hydrophobic spacing layers (PMMA) between the perovskite/ETL heterointerface.

We started this study inspired by the insight that the dynamic motion of Nd ion within the fullerene cage and the strong Nd-cage interaction could facilitate ultrafast intramolecular ET. This phenomenon is expected to create shortened intramolecular transfer channels and electromagnetic-coupled transmitters. In this context, we have focused on achieving homogeneous ultrafast electron extraction at the perovskite/ETL interface for inverted PSCs by developing an Nd-based endohedral metallofullerene ESL. The endohedral metallofullerene–polymer coupling ESL (Nd@C$_{82}$–PMMA) demonstrated not only ultrafast carrier extraction but also enhanced stability. This improvement was achieved through the permanent strong electric field generated by the polarized Nd@C$_{82}$ interface, which promotes efficient carrier separation and extraction, whereas the interpenetrating network of PMMA further suppresses ion interdiffusion. The reduction of insufficient carrier extraction-induced recombination results in efficient, stable and scalable production of inverted PSCs and modules. We believe that the strategy of endohedral metallofullerene–polymer coupling ESL combining with advanced large-area deposition technology is universally useful for other perovskite-based devices in practical applications.

Online content

Any methods, additional references, Nature Portfolio reporting summaries, source data, extended data, supplementary information, acknowledgements, peer review information; details of author contributions and competing interests; and statements of data and code availability are available at https://doi.org/10.1038/s41586-025-08961-9.

1. Peng, J. et al. Nanoscale localized contacts for high fill factors in polymer-passivated perovskite solar cells. *Science* **371**, 390–395 (2021).
2. Peng, J. et al. Centimetre-scale perovskite solar cells with fill factors of more than 86 per cent. *Nature* **601**, 573–578 (2022).
3. Zhao, Y. et al. A polymer scaffold for self-healing perovskite solar cells. *Nat. Commun.* **7**, 10228 (2016).
4. Chen, H. et al. Improved charge extraction in inverted perovskite solar cells with dual-site-binding ligands. *Science* **384**, 189–193 (2024).
5. Liu, C. et al. Bimolecularly passivated interface enables efficient and stable inverted perovskite solar cells. *Science* **382**, 810–815 (2023).
6. Yoo, J. J. et al. Efficient perovskite solar cells via improved carrier management. *Nature* **590**, 587–593 (2021).
7. Liu, S. et al. Buried interface molecular hybrid for inverted perovskite solar cells. *Nature* **632**, 536–542 (2024).
8. Zhang, S. et al. Minimizing buried interfacial defects for efficient inverted perovskite solar cells. *Science* **380**, 404–409 (2023).
9. Yu, S. et al. Homogenized NiO$_x$ nanoparticles for improved hole transport in inverted perovskite solar cells. *Science* **382**, 1399–1404 (2023).
10. Shen, Z. et al. Efficient and stable perovskite solar cells with regulated depletion region. *Nat. Photon.* **18**, 450–457 (2024).
11. Tang, H. et al. Reinforcing self-assembly of hole transport molecules for stable inverted perovskite solar cells. *Science* **383**, 1236–1240 (2024).
12. Park, S. M. et al. Low-loss contacts on textured substrates for inverted perovskite solar cells. *Nature* **624**, 289–294 (2023).
13. Chen, P. et al. Multifunctional ytterbium oxide buffer for perovskite solar cells. *Nature* **625**, 516–522 (2024).
14. Han, T.-H. et al. Perovskite-polymer composite cross-linker approach for highly-stable and efficient perovskite solar cells. *Nat. Commun.* **10**, 520 (2019).
15. Jiang, Y. et al. Reduction of lead leakage from damaged lead halide perovskite solar modules using self-healing polymer-based encapsulation. *Nat. Energy* **4**, 585–593 (2019).
16. Luo, J. et al. Polymer-acid-metal quasi-ohmic contact for stable perovskite solar cells beyond a 20,000-hour extrapolated lifetime. *Nat. Commun.* **15**, 2002 (2024).
17. Said, A. A. et al. Sublimed C$_{60}$ for efficient and repeatable perovskite-based solar cells. *Nat. Commun.* **15**, 708 (2024).
18. Chen, J. et al. Efficient tin-based perovskite solar cells with trans-isomeric fulleropyrrolidine additives. *Nat. Photon.* **18**, 464–470 (2024).
19. Ren, X. et al. Mobile iodides capture for highly photolysis- and reverse-bias-stable perovskite solar cells. *Nat. Mater.* **23**, 810–817 (2024).
20. Li, Z. et al. Stabilized hole-selective layer for high-performance inverted p-i-n perovskite solar cells. *Science* **382**, 284–289 (2023).
21. Xu, J. et al. Anion optimization for bifunctional surface passivation in perovskite solar cells. *Nat. Mater.* **22**, 1507–1514 (2023).
22. Khenkin, M. V. et al. Consensus statement for stability assessment and reporting for perovskite photovoltaics based on ISOS procedures. *Nat. Energy* **5**, 35–49 (2020).
23. Lin, N. et al. STM investigation of metal endohedral fullerene adsorbed on a Van der Waals surface. *Phys. Lett. A* **222**, 190–194 (1996).
24. Akiyama, K. et al. Absorption spectra of metallofullerenes M@C$_{82}$ of lanthanoids. *J. Phys. Chem. A* **104**, 7224–7226 (2000).
25. Zhang, Y. et al. Favorite orientation of the carbon cage and a unique two-dimensional-layered packing model in the cocrystals of Nd@C$_{82}$(I,II) isomers with decapyrrylcorannulene. *Inorg. Chem.* **60**, 1462–1471 (2021).
26. Wu, B.-S. et al. Radiation-processed perovskite solar cells with fullerene-enhanced performance and stability. *Cell Reports Phys. Sci.* **2**, 100646 (2021).
27. Naaman, R. et al. New perspective on electron transfer through molecules. *J. Phys. Chem. Lett.* **13**, 11753–11759 (2022).
28. Ding, J., Lin, N., Weng, L.-T., Cue, N. & Yang, S. Isolation and characterization of a new metallofullerene Nd@C$_{82}$. *Chem. Phys. Lett.* **261**, 92–97 (1996).
29. Jang, Y. W. et al. Intact 2D/3D halide junction perovskite solar cells via solid-phase in-plane growth. *Nat. Energy* **6**, 63–71 (2021).
30. Kresse, G. et al. From ultrasoft pseudopotentials to the projector augmented-wave method. *Phys. Rev. B* **59**, 1758–1775 (1999).
31. Olthof, S. et al. Ultralow doping in organic semiconductors: evidence of trap filling. *Phys. Rev. Lett.* **109**, 176601 (2012).
32. Gong, Y. et al. Boosting exciton mobility approaching Mott-Ioffe-Regel limit in Ruddlesden–Popper perovskites by anchoring the organic cation. *Nat. Commun.* **15**, 1893 (2024).
33. Zhang, H. et al. Lead immobilization for environmentally sustainable perovskite solar cells. *Nature* **617**, 687–695 (2023).

34. Ding, B. et al. Dopant-additive synergism enhances perovskite solar modules. *Nature* **628**, 299–305 (2024).
35. Zhao, Y. et al. Perovskite seeding growth of formamidinium-lead-iodide-based perovskites for efficient and stable solar cells. *Nat. Commun.* **9**, 1607 (2018).
36. Huang, Z. et al. Anion–π interactions suppress phase impurities in $FAPbI_3$ solar cells. *Nature* **623**, 531–537 (2023).
37. Chen, Y. et al. Molecular design and morphology control towards efficient polymer solar cells processed using non-aromatic and non-chlorinated solvents. *Adv. Mater.* **26**, 2744–2749 (2014).
38. Kirchartz, T. et al. Efficiency limits of organic bulk heterojunction solar cells. *J. Phys. Chem. C* **113**, 17958–17966 (2009).
39. Jiang, Q. et al. Surface reaction for efficient and stable inverted perovskite solar cells. *Nature* **611**, 278–283 (2022).
40. Sun, H. et al. Scalable solution-processed hybrid electron transport layers for efficient all-perovskite tandem solar modules. *Adv. Mater.* **36**, 2308706 (2024).

Methods

Materials

All the solvents and reagents were purchased and used without further purification. Patterned indium tin oxide (ITO) glass was purchased from Advanced Election Technology. Lead iodide (PbI_2, 99.99%, trace metals basis) was purchased from TCI Chemicals. Formamidinium iodide (FAI, ≥99.5%) and methylammonium chloride (MACl, ≥99.5%) were purchased from Greatcell. Phenylethylamine chloride (PEACl, 99.5%), C_{60} and lead chloride ($PbCl_2$, 99.99%) were obtained from Xi'an Polymer Light Technology. (2-(4-(bis(4-Methoxyphenyl)amino) phenyl)-1-cyanovinyl)phosphonic acid (MPA-CPA) was purchased from Borun New Material. Graphite rods and graphite powder were purchased from Shanghai Fengyi Carbon. Neodymium(III)-oxide (Nd_2O_3, 99.99% metal basis) was purchased from Meryer. CS_2 (for HPLC, ≥99%) was purchased from Aladdin. Toluene (≥99.8%) was purchased from Xilong Science. Dimethylformamide (DMF, 99.8%), dimethyl sulfoxide (DMSO, 99.9%), chlorobenzene (CB, 99.9%), isopropanol (IPA, 99.9%) and anhydrous ethanol (EtOH, 99%) were obtained from Acros Organics.

Fabrication of small-area device

The inverted (p-i-n) perovskite solar cells studied in this work were an architecture of ITO/MPA-CPA/perovskite/$Nd@C_{82}$/C_{60}/BCP/Ag. Glass/ITO substrates were sequentially cleaned with detergent (2% in deionized water), deionized water and EtOH, by sonication for 20 min in each solution. Then the cleaned substrates were dried in a drying cabinet and treated with UV ozone for 20 min before use. The MPA-CPA (1 mg ml^{-1} in IPA) solution was subjected to spin-coating on the substrate at 3,000 rpm for 30 s and annealed at 100 °C for 10 min. The as-prepared ITO/MPA-CPA was stored in a glovebox at room temperature for over 12 h. For the preparation of perovskite precursor solution, 1.7 M $Cs_{0.05}MA_{0.05}FA_{0.90}PbI_3$ perovskite precursor in DMF:DMSO (4:1 volume ratio, v:v) was treated with 5% $MAPbCl_3$ excess. The as-prepared perovskite precursor was subjected to spin-coating onto the MPA-CPA-coated ITO substrates at 1,000 rpm for 10 s (acceleration rate 200 rpm s^{-1}) and 5,500 rpm for 30 s (acceleration rate 1,000 rpm s^{-1}), respectively. At 20 s of the second step, 200 µl mixed antisolvent (chlorobenzene: isopropanol = 9:1, v:v, containing 1 mg/ml PEACl) was slowly dripped onto the centre of the film at 10 s before the end of the spinning. The perovskite film was obtained by annealing at 100 °C for 10 min. After cooling to room temperature, the interface layer was subjected to spin-coating with $Nd@C_{82}$:PMMA dissolved in CB (1.0 mg ml^{-1}:1.0 mg ml^{-1}) at 2,000 rpm for 10 s, and this step was repeated thrice. Finally, 20 nm of C_{60}, 7 nm of BCP and 100 nm of silver electrode were thermally evaporated.

Module fabrication

The cleaned ITO substrates (5 × 5 cm) were first subjected to laser scribing to form P1, using a 532-nm green laser to delineate six sub-ITO regions on a 5 × 5 cm ITO substrate. The specific operational parameters were as follows: an average laser power of 15.4 W, a spot diameter of 25 µm, a pulse frequency of 110 kHz, a scribing velocity of 800 mm s^{-1} and a scribing linewidth of 100 µm. Following the scribing process, the ITO substrates were sequentially cleaned with detergent (2% in deionized water), deionized water and EtOH, by sonication for 20 min in each solution. Then the cleaned substrates were dried in a drying cabinet and treated with UV ozone for 20 min before use. Subsequently, a solution of SAM (1 mg ml^{-1} in IPA) was subjected to spin-coating onto the ITO at 3,000 rpm for 30 s, followed by annealing at 100 °C for 10 min. The as-prepared ITO/SAM was stored in a glovebox at room temperature for over 12 h. The as-prepared perovskite precursor was subjected to spin-coating onto the SAM-coated ITO substrates at 1,000 rpm for 10 s (acceleration rate 200 rpm s^{-1}) and 5,500 rpm for 30 s (acceleration rate 1,000 rpm s^{-1}), respectively. At 20 s of the second step, 1,000 µl mixed antisolvent (chlorobenzene: isopropanol = 9:1, v:v, containing 1 mg ml^{-1} PEACl) was slowly dripped onto the centre of the film at 10 s before the end of the spinning. The resulting film underwent annealing at 100 °C for 10 min. After that, the interface layer was subjected to spin-coating with $Nd@C_{82}$:PMMA dissolved in CB (1.0 mg ml^{-1}:1.0 mg ml^{-1}) at 2,000 rpm for 10 s, and this step was repeated thrice, and 20 nm of C_{60} and 7 nm of BCP were thermally evaporated. After the deposition of the BCP, the sample was scribed to form P2, using the aforementioned laser scribing device with the following parameters: an average laser power of 16.8 W, a spot diameter of 25 µm, a pulse frequency of 120 kHz, a scribing velocity of 800 mm s^{-1} and a scribing linewidth of 100 µm, repeated twice. Then, 110 nm of copper (Cu) electrode was thermally evaporated. Finally, monolithically interconnected modules were formed by laser scribing to form P3, using the aforementioned laser scribing device, with parameters set to an average laser power of 19.6 W, a spot diameter of 25 µm, a pulse frequency of 140 kHz, a scribing velocity of 600 mm s^{-1} and a scribing linewidth of 100 µm, repeated twice. Through meticulous execution of these processing steps, a 5 × 5 cm perovskite solar cell module, comprising six series-connected subcells, was successfully fabricated. All the directions of scribes created by the laser were unidirectional and from the top of the module to the bottom.

Film characterization

Scanning electron microscopy images were obtained using a field emission scanning electron microscope (SEM, JEOL-JSM7800F). XRD patterns of all perovskite films were characterized using an X-ray diffractometer (XRD, Bruker D8 Advance) at a scan rate of 10° min^{-1}. The grazing-incidence wide-angle X-ray scattering (GIWAXS) was performed at the BL02U beamline of the Shanghai Synchrotron Radiation Facility (SSRF) using an X-ray with an energy of 9.99881 keV. Steady-state photoluminescence (PL) spectra were measured by Princeton Instruments. PL mapping measurements were conducted by the instrument Vis–NIR–XU (Nanophoton) with excitation at 532 nm. Time-resolved photoluminescence (TRPL) was conducted with a universal streak camera (Hamamatsu). Ultraviolet–visible (UV–Vis) spectra were acquired on a Shimadzu UV 1750 spectrophotometer at room temperature. An atomic force microscope (AFM; SPM-9700HT) was used to collect AFM and KPFM images. XPS measurements were performed on a Scientific ESCALAB Xi+ Al Kα (1,486.6 eV) radiation. A 500-µm X-ray spot was used for XPS analysis. Ultraviolet photoelectron spectroscopy (UPS) depth profiling measurement was also carried out on a Scientific ESCALAB Xi+, with the HeI (21.22 eV) emission line used for excitation. TEM lamellae are extracted and thinned down using a focused ion beam (Thermo Scientific Helios 5 UX) at 30 kV and finally polished at 5 kV. To protect the region of interest during ion beam processing, a Pt layer was deposited for protection. Transmission electron microscopy images were recorded using JEM-ARM300F2 at 300 kV. The dielectric properties were tested using the precision impedance analyser (4294A, Agilent).

Device characterization

Current density–voltage (*J*–*V*) curves were tested on a Keysight B2901B source/meter unit in a solar simulator (Enlitech SS-X100) after calibrating the light intensity to AM 1.5G one sun (100 mW cm^{-2}) in a standard silicon solar cell calibrated by Newport under AM 1.5G standard light. Current–voltage curves were measured in the forward scan range of −0.1 V to 1.2 V and the reverse scan from 1.2 V to −0.1 V. All the devices were tested using a black metal aperture with a mask area of 0.08 cm^2 for the devices. The *J*–*V* measurements of non-encapsulated solar cells were performed in an N_2-filled glovebox. The conductance and defect density were tested according to our previous work[41]. The external quantum efficiency (EQE) was measured by a solar cell spectral response measurement system (QE-R3018, Enli Technology) with the light intensity calibrated by a standard single-crystal Si photovoltaic cell. Electrochemical impedance spectroscopy (EIS) measurement was performed on a Princeton electrochemical workstation

(ChenHua, CHI760E, Chana) in the frequency range of 0.1–100,000 Hz, and the applied bias voltage was set at 0 V. The devices were subjected to long-term light stability tests in a nitrogen glovebox under white LEDs, tested periodically by a solar simulator. For the stability tests, the Ag electrode was replaced by 110 nm Cu films deposited by thermal evaporation. For ISOS-D-2I thermal stability tests, the cells were heated at 85 °C in nitrogen. The performance of the device was tested periodically. For the ISOS-L-3 ageing test, devices were placed in a custom-made stability-tracking station. The device chamber was left open in a room with 50 ± 10% relative humidity, and the solar cell was mounted on a metal plate kept at 65 °C using a heating element. The illumination source is a white-light LED with its intensity calibrated to match 1-sun conditions. TOF-SIMS and ion images were collected using Bi^{3+} ion beam accelerated at 30 keV and Ar accelerated at 10 keV. The analysing area was $100 \times 100\ \mu m^2$, and the sputter-beam centre area was $250 \times 300\ \mu m^2$ in the frequency range of 0.1–100,000 Hz, and the applied bias voltage was set at 0 V. The devices were subjected to long-term light stability tests in a nitrogen glovebox under white LEDs, tested periodically by a solar simulator. For ISOS-D-3 damp heat stability tests, the encapsulated devices were placed in the environmental test chamber at 85 °C/85% relative humidity and the PCEs were measured periodically after the devices cooled to room temperature. The encapsulation method of the PSCs was processed according to a previous report[42].

Other characterization

Mass spectra were recorded by the Autoflex III amartbeam (Bruker, Germany) coupled with a MALDI source. The Vis–NIR spectra of the purified Nd@C_{82} samples in a toluene solution were measured with a UV–vis–NIR spectrometer (PE Lambda950, China). The EPR spectra of the purified Nd@C_{82} samples were measured with an EPR spectrometer (Bruker A300-9.5/12, Germany).

Computation

The density functional theory (DFT) calculations of magnetic moment in this work were carried out with the Vienna ab initio simulation package[43] at the level of the spin-polarized generalized-gradient approximation in the form of Perdew–Burke–Enzerhof (PBE) functional[44–46]. The interaction between valence electrons and ionic cores was considered within the framework of the projector augmented wave method[30,47]. The energy cutoff for the plane wave basis expansion was set at 400 eV. The van der Waal's correction (DFT D3) was included in all calculations[48,49]. The criterion for total energy convergence was set at 10^{-4} eV. Owing to the presence of the heavy element lead, spin–orbit coupling effects are considered in all calculations related to perovskites. The highest occupied molecular orbital and the lowest unoccupied molecular orbital energy levels of Nd@C_{82} were carried out using Gaussian 09 program package with PBE0 method[50]. The def2-TZVP basis sets were used for Nd, and the 6–31G** basis set was used for C. According to the previous findings, PBE0 is an appropriate method that was used to calculate lanthanide complex systems[51,52].

Electronic conductivity is rigorously quantified by leveraging the Boltzmann transport equation in harmony with the relaxation time approximation[30]. This approach ensures a robust calculation of transport phenomena within the crystalline lattice. The band velocity, denoted as $\mathbf{v}_\alpha(\mathbf{i},\mathbf{k})$, is defined as the gradient of the energy eigenvalues with respect to the crystal wave vector ($\mathbf{k}$):

$$\mathbf{v}_\alpha(\mathbf{i},\mathbf{k}) = \frac{1}{\hbar}\frac{\partial \boldsymbol{\varepsilon}_{\mathbf{i},\mathbf{k}}}{\partial \mathbf{k}_\alpha}$$

In this context, $\boldsymbol{\varepsilon}(\mathbf{i},\mathbf{k})$ signifies the energy associated with the ith band at wave vector $\mathbf{k}$, and the subscript α represents a specified Cartesian coordinate axis. This foundational understanding facilitates the derivation of the electrical conductivity tensor component ($\boldsymbol{\sigma}_{\alpha\beta}(\mathbf{i},\mathbf{k})$), using the relationship

$$\boldsymbol{\sigma}_{\alpha\beta}(\mathbf{i},\mathbf{k}) = e^2 \boldsymbol{\tau}_{\mathbf{i},\mathbf{k}} \mathbf{v}_\alpha(\mathbf{i},\mathbf{k}) \mathbf{v}_\beta(\mathbf{i},\mathbf{k})$$

Here, $\boldsymbol{\tau}(\mathbf{i},\mathbf{k})$ captures the relaxation time, indicating the timescale pertinent to scattering events in the electronic band structure. The group velocity along the β axis is articulated by ($\mathbf{v}_\beta(\mathbf{i},\mathbf{k})$). Relaxation time emerges as a pivotal factor, intricately capturing the complex interplay of various scattering mechanisms that decisively influence the lifetimes of charge carriers.

To obtain a macroscopic representation of electrical conductivity, denoted by ($\boldsymbol{\sigma}_{\alpha\beta}(T,\mu)$), for a material at a given temperature T and chemical potential μ, we integrate the microscopic conductivity across the energy spectrum. This integration is not merely a mathematical procedure but an aggregation of the myriad contributions from charge carriers, each occupying distinct energy states. This collective amalgamation offers an exhaustive depiction of the conductive attributes of the material:

$$\boldsymbol{\sigma}_{\alpha\beta}(T,\mu) = \frac{1}{\Omega}\int \boldsymbol{\sigma}_{\alpha\beta}(\varepsilon)\left(-\frac{\partial f(T,\varepsilon)}{\partial \varepsilon}\right)d\varepsilon$$

The above formulations are crucial in the theoretical exploration of electronic transport and provide a comprehensive framework for understanding and predicting material behaviour under various thermoelectric conditions.

Reporting summary

Further information on research design is available in the Nature Portfolio Reporting Summary linked to this article.

Data availability

All data are available in the main text or supplementary materials. The data that support the findings of this study are available from the corresponding authors upon reasonable request. Source data are provided with this paper.

41. Yang, W. et al. Tailoring component incorporation for homogenized perovskite solar cells. *Sci. Bull.* **69**, 2555–2564 (2024).
42. Lin, R. et al. All-perovskite tandem solar cells with 3D/3D bilayer perovskite heterojunction. *Nature* **620**, 994–1000 (2023).
43. Kresse, G. et al. Efficiency of ab-initio total energy calculations for metals and semiconductors using a plane-wave basis set. *Comput. Mater. Sci.* **6**, 15–50 (1996).
44. Kresse, G. Efficient iterative schemes for ab initio total-energy calculations using a plane-wave basis set. *Phys. Rev. B* **50**, 17953–17979 (1994).
45. Perdew, J. P. et al. Generalized gradient approximation made simple. *Phys. Rev. Lett.* **77**, 3865–3868 (1996).
46. Dalpian, G. M., Zhao, X,-G., Kazmerski, L. & Zunger, A. Formation and composition-dependent properties of alloys of cubic halide perovskites. *Chem. Mater.* **31**, 2497–2506 (2019).
47. Blöchl, P. E. Projector augmented-wave method. *Phys. Rev. B* **50**, 17953–17979 (1994).
48. Grimme, S., Ehrlich, S. & Goerigk, L. Effect of the damping function in dispersion corrected density functional theory. *J. Comput. Chem.* **32**, 1456–1465 (2011).
49. Grimme, S., Antony, J., Ehrlich, S. & Krieg, H. A consistent and accurate ab initio parametrization of density functional dispersion correction (DFT-D) for the 94 elements H-Pu. *J. Chem. Phys.* **132**, 154104 (2010).
50. Frisch, M. J. et al. Gaussian 09 Revision D.01 (Gaussian, 2009).
51. Chen, X. et al. Lanthanides with unusually low oxidation states in the PrB_3^- and PrB_4^- boride clusters. *Inorg. Chem.* **58**, 411–418 (2019).
52. Pantazis, D. A., & Neese, F. All-electron scalar relativistic basis sets for the lanthanides. *J. Chem. Theory Comput.* **5**, 2229–2238 (2009).

Acknowledgements S.Y. and C.L. thank the Core Facilities Sharing Platform of Xi'an Jiaotong University (XJTU) for performing various characterizations; Y.L. and C.L. thank the staff from the BL02U beamline of the Shanghai Synchrotron Radiation Facility (SSRF) for assistance during data collection. We thank Y. Liang, H. Guo and Y. Zhang at the Instrument Analysis Center of Xi'an Jiaotong University for their assistance with TOF-SIMS, KPFM and HR-TEM analyses, respectively. We also thank the National Key Research and Development Program of China (2024YFE0201800), the National Natural Science Foundation of China (62304111, 22201227, 12274337, U1866203, 92066207, 62175268, 52472199), the Shaanxi Fundamental Science Research Project for Mathematics and Physics (22JSY015, 23JSY005), the Young Talent Fund of Xi'an Association for Science and Technology (959202313020), the Shaanxi Province science and technology activities for overseas students selected funding project (2023015), the State

Key Laboratory for Strength and Vibration of Mechanical Structures (SV2023-KF-18), the youth project in natural science and engineering technology (2023SYJ15), the Project of State Key Laboratory of Organic Electronics and Information Displays, the Qin Chuang Yuan Program of Shaan Xi Province (grant no. 2021QCYRC4-37), the Nanjing University of Posts and Telecommunications (GZR2023010046), the Natural Science Research Start-up Foundation of Recruiting Talents of Nanjing University of Posts and Telecommunications (NY223053), the China Fundamental Research Funds for the Central Universities, the China Postdoctoral Science Foundation (grant no. 2022M721026), the Joint Fund of Provincial Science, and Technology Research and Development Plan of Henan Province (Grant No. 232301420004), the Science and Technology Development Fund, Macao SAR (file no. 0010/2022/AMJ, 0060/2023/RIA1, 006/2022/ALC, 0122/2024/AMJ), the research fund of UM (file no. MYRG-GRG2023-00065-IAPME-UMDF).

Author contributions W.C., T.Y., M.L., S.Y. and C.L. conceptualized the study; Y.L., Z.L., S.L., T. Liu, W.M., Y.S. and C.L. devised the methodology; Y.L., Z.L., S.L., Y.S., W.Z., Z.Z., J.Z., W.Y., H.G., J.X., D.W., F.D., A.Z., J.L., H.C., B.W., N.Z., H.W., X.L., T. Li, C.K., D.Z., S.C. and Z.Y. conducted the investigation; Y.L., S.L., Y.S. and W.Y. performed the visualization; S.Y., M.L. and C.L. helped with funding acquisition; W.C., S.Y., M.L. and C.L. helped with the project administration; G.X., S.Y., T.Y., W.C., M.L., W.H., and C.L. supervised the study; Y.L. and C.L. wrote the original draft; G.F., L.E., G.X., W.C., T.Y., S.Y., M.L. and C.L. wrote, reviewed and edited the paper. All authors discussed the results and commented on the paper.

Competing interests The authors declare no competing interests.

Additional information

Supplementary information The online version contains supplementary material available at https://doi.org/10.1038/s41586-025-08961-9.

Correspondence and requests for materials should be addressed to Guichuan Xing, Shengchun Yang, Tao Yang, Wenting Cai, Meng Li or Chao Liang.

Peer review information *Nature* thanks Ana Montero-Alejo, Jae Yun and the other, anonymous, reviewer(s) for their contribution to the peer review of this work.

nature portfolio

Corresponding author(s): Guichuan Xing, Shengchun Yang, Tao Yang, Wenting Cai, Meng Li, Chao Liang

Solar Cells Reporting Summary

Nature Portfolio wishes to improve the reproducibility of the work that we publish. This form is intended for publication with all accepted papers reporting the characterization of photovoltaic devices and provides structure for consistency and transparency in reporting. Some list items might not apply to an individual manuscript, but all fields must be completed for clarity.

For further information on Nature Research policies, including our data availability policy, see Authors & Referees.

Experimental design

Please check the following details are reported in the manuscript, and provide a brief description or explanation where applicable.

1. Dimensions

Area of the tested solar cells	☒ Yes ☐ No	Aperture areas of 0.08 and 16 cm2 were used in this work. *Explain why this information is not reported/not relevant.*
Method used to determine the device area	☒ Yes ☐ No	Black metal aperture masks were used during the J-V measurements. *Explain why this information is not reported/not relevant.*

2. Current-voltage characterization

Current density-voltage (J-V) plots in both forward and backward direction	☒ Yes ☐ No	Provided in this manuscript.
Voltage scan conditions	☒ Yes ☐ No	Provided in Method section. *Explain why this information is not reported/not relevant.*
Test environment	☒ Yes ☐ No	Provided in Method section. *Explain why this information is not reported/not relevant.*
Protocol for preconditioning of the device before its characterization	☐ Yes ☒ No	*Provide a description of the protocol.* No preconditioning was used in this work.
Stability of the J-V characteristic	☒ Yes ☐ No	Stabilized PCEs of solar cells were provided. *Explain why this information is not reported/not relevant.*

3. Hysteresis or any other unusual behaviour

Description of the unusual behaviour observed during the characterization	☒ Yes ☐ No	Very minor hysteresis was observed for devices herein. *Explain why this information is not reported/not relevant.*
Related experimental data	☒ Yes ☐ No	J-V curves under reverse and forward scans were provided. *Explain why this information is not reported/not relevant.*

4. Efficiency

External quantum efficiency (EQE) or incident photons to current efficiency (IPCE)	☒ Yes ☐ No	EQE curves were provided. *Explain why this information is not reported/not relevant.*
A comparison between the integrated response under the standard reference spectrum and the response measure under the simulator	☒ Yes ☐ No	The integrated Jsc values from QE were consistent with Jsc values from J-V measurements. *Explain why this information is not reported/not relevant.*

For tandem solar cells, the bias illumination and bias voltage used for each subcell	☐ Yes ☒ No	*Provide a description of the measurement conditions.* N.A.

5. Calibration

Light source and reference cell or sensor used for the characterization	☒ Yes ☐ No	Stated in Method section. *Explain why this information is not reported/not relevant.*
Confirmation that the reference cell was calibrated and certified	☒ Yes ☐ No	The reference cells were calibrated by Newport and explained in Method. *Explain why this information is not reported/not relevant.*
Calculation of spectral mismatch between the reference cell and the devices under test	☐ Yes ☒ No	*Provide a value of the spectral mismatch and/or a description of how it has been taken into account in the measurements.* The light spectrum used for measurements matches well with the reference silicon cell, and we did not calculate the spectral mismatch between the reference cell and the tested devices.

6. Mask/aperture

Size of the mask/aperture used during testing	☒ Yes ☐ No	Aperture areas of 0.08 and 16 cm2 were used in this work. *Explain why this information is not reported/not relevant.*
Variation of the measured short-circuit current density with the mask/aperture area	☐ Yes ☒ No	*Report the difference in the short-circuit current density values measured with the mask and aperture area.* We measured all devices with masks.

7. Performance certification

Identity of the independent certification laboratory that confirmed the photovoltaic performance	☒ Yes ☐ No	Measured by an independently accredited testing center (FuJian Metrology Institute (National PV Industry Measurement and Testing Center and Shanghai Institute of Microsystem and Information Technology), Supplementary Figure 49 and 50. *Explain why this information is not reported/not relevant.*
A copy of any certificate(s)	☒ Yes ☐ No	Supplementary Figure 49 and 50. *Explain why this information is not reported/not relevant.*

8. Statistics

Number of solar cells tested	☒ Yes ☐ No	We tested 15 cells. *Explain why this information is not reported/not relevant.*
Statistical analysis of the device performance	☐ Yes ☒ No	*State where this information can be found in the text.* No significant variations were observed.

9. Long-term stability analysis

Type of analysis, bias conditions and environmental conditions	☒ Yes ☐ No	Stated in Method section. *Explain why this information is not reported/not relevant.*